Andrew F. Nagy • André Balogh • Thomas E. Cravens •
Michael Mendillo • Ingo Mueller-Wodarg
Editors

Comparative Aeronomy

Previously published in *Space Science Reviews* Volume 139,
Issues 1–4, 2008

Springer

Andrew F. Nagy
Dept. of Atmospheric, Oceanic and
Space Sciences
University of Michigan
Ann Arbor, MI, USA

André Balogh
Internation Space Science Institute
Bern, Switzerland

Thomas E. Cravens
Dept. of Physics and Astronomy
University of Kansas
Lawrence, KS, USA

Michael Mendillo
Department of Astronomy
Boston University
Boston, MA, USA

Ingo Mueller-Wodarg
Space and Atmospheric Physics Group
The Blackett Laboratory
Imperial College London
London, UK

Cover illustration: Courtesy NASA/JPL-Caltech

Library of Congress Control Number: 2008939139

ISBN-978-0-387-87824-9 e-ISBN-978-0-387-87825-6

Printed on acid-free paper.

1

springer.com

Contents

Preface

Andrew F. Nagy

Originally published in the journal Space Science Reviews, Volume 139, Nos 1–4.
DOI: 10.1007/s11214-008-9353-0

Keywords Aeronomy

The term "aeronomy" has been used widely for many decades, but its origin has mostly been lost over the years. It was introduced by Sydney Chapman in a Letter to the Editor, entitled "Some Thoughts on Nomenclature", in *Nature* in 1946 (Chapman 1946). In that letter he suggested that aeronomy should replace meteorology, writing that the word "meteor is now irrelevant and misleading". This proposal was apparently not received with much support so in a short note in Weather in 1953 Chapman (1953) wrote:

> "If, despite its obvious convenience of brevity in itself and its derivatives, it does not commend itself to aeronomers, I think there is a case for modifying my proposal so that instead of the word being used to signify the study of the atmosphere in general, it should be adopted with the restricted sense of the science of the *upper* atmosphere, for which there is no convenient short word."

In a chapter, he wrote in a 1960 book (Chapman 1960), he give his final and definitive definition, by stating that "Aeronomy is the science of the upper region of the atmosphere, where dissociation and ionization are important".

The Workshop on "Comparative Aeronomy" was held at ISSI during the week of June 25–29, 2007. Participation of this workshop was by invitation only due to space limitations at the available meeting facility. The structure of the meeting was such that each of the 32 selected topic was allocated a 30 minute presentation, which was then followed by 20 minutes of open discussion. This book is based on those presentations, but is not a collection of the talks, but is a synthesis, presented as 11 chapters.

This was the second week-long conference dealing with this topic; the first with the same title was held as a Chapman Conference at the Yosemite National Park during February

A.F. Nagy (✉)
Department of Atmospheric, Oceanic and Space Sciences, University of Michigan, Ann Arbor, MI 48109, USA
e-mail: anagy@umich.edu

8–11, 2000 (Mendillo et al. 2002). A full-day symposium on comparative aeronomy was subsequently sponsored by the Royal Astronomical Society in London in January 2003. These meetings, and some preceding CEDAR Workshops, have clearly established that there is a great deal of similarity in the physical and chemical processes controlling the various upper atmospheres and ionospheres in the solar system. Yet, there are significant differences as well due to such factors as distance from the Sun, different neutral atmospheres, roles of intrinsic and induced magnetic fields, and the presence of a surface or regolith of the object under study. Therefore it has become quite clear that there is a great deal to be learned by discussions among scientists working on different aeronomical problems in diverse settings in our Solar System and, increasingly, on extra-solar-system planets. This ISSI workshop addressed all of these topics in a venue that fostered comparisons and syntheses.

References

S. Chapman, Some thoughts on nomenclature. Nature **157**, 105 (1946)
S. Chapman, Nomenclature in meteorology. Weather **7–8**, 62 (1953)
S. Chapman, The thermosphere – The Earth's outermost atmosphere, in *Physics of the Upper Atmosphere*, ed. by J.A. Ratcliffe (Academic Press, 1960)
M. Mendillo, A. Nagy, J.H. Waite (eds.), *Atmospheres in the Solar System: Comparative Aeronomy* (American Geophysical Union, 2002)

Energy Deposition in Planetary Atmospheres by Charged Particles and Solar Photons

Jane L. Fox · Marina I. Galand · Robert E. Johnson

Originally published in the journal Space Science Reviews, Volume 139, Nos 1–4.
DOI: 10.1007/s11214-008-9403-7

Abstract We discuss here the energy deposition of solar FUV, EUV and X-ray photons, energetic auroral particles, and pickup ions. Photons and the photoelectrons that they produce may interact with thermospheric neutral species producing dissociation, ionization, excitation, and heating. The interaction of X-rays or keV electrons with atmospheric neutrals may produce core-ionized species, which may decay by the production of characteristic X-rays or Auger electrons. Energetic particles may precipitate into the atmosphere, and their collisions with atmospheric particles also produce ionization, excitation, and heating, and auroral emissions. Auroral energetic particles, like photoelectrons, interact with the atmospheric species through discrete collisions that produce ionization, excitation, and heating of the ambient electron population. Auroral particles are, however, not restricted to the sunlit regions. They originate outside the atmosphere and are more energetic than photoelectrons, especially at magnetized planets. The spectroscopic analysis of auroral emissions is discussed here, along with its relevance to precipitating particle diagnostics. Atmospheres can also be modified by the energy deposited by the incident pickup ions with energies of eV's to MeV's; these particles may be of solar wind origin, or from a magnetospheric plasma. When the modeling of the energy deposition of the plasma is calculated, the subsequent modeling of the atmospheric processes, such as chemistry, emission, and the fate of hot recoil particles produced is roughly independent of the exciting radiation. However, calculating the spatial distribution of the energy deposition versus depth into the atmosphere produced by an incident plasma is much more complex than is the calculation of the solar excitation profile. Here, the nature of the energy deposition processes by the incident plasma are described as is the fate of the hot recoil particles produced by exothermic chemistry and by knock-on collisions by the incident ions.

J.L. Fox (✉)
Wright State University, Dayton, USA
e-mail: jane.fox@wright.edu

M.I. Galand
Imperial College, London, England

R.E. Johnson
University of Virginia, Charlottesville, USA

Keywords Energy deposition · Photon absorption · Chapman functions · Heating efficiencies · Auger electrons · Characteristic X-rays · X-ray absorption · Doubly charged ions · Core-excited ions · Auroral electrons · Auroral emissions · Color ratios · Auroral particles · Heavy ions · Electron transport · Pickup ions · Range of energetic particles · Knock-on · Recoil particles · Energy loss per ion pair

1 Introduction

The source for nearly all atmospheric processes is ultimately the interaction of solar photons and energetic particles of solar or magnetospheric origin with the atmosphere. We discuss first the energy deposition of solar FUV, EUV and X-ray photons. These photons and the photoelectrons that they produce may interact with thermospheric neutral species producing dissociation, ionization, excitation, and heating. The interaction of X-rays or keV electrons with atmospheric neutrals may produce ejection of inner shell electrons. The resulting core-ionized species may decay by the production of characteristic X-rays or Auger electrons.

Energetic particles may precipitate into the atmosphere, producing auroral emissions. Auroral energetic particles, like photoelectrons, interact with the atmospheric species through collisions that produce ionization, excitation, and heating of the ambient electron population. Auroral particles are, however, not restricted to the sunlit regions. They originate outside the atmosphere and are more energetic than photoelectrons, especially at the magnetized planets. Their spectral shape is very different from those of photoelectrons. The focus here is on the spectroscopic analysis of auroral emissions, their relevance to precipitating particle diagnostics, and the similarities and differences of such an approach applied to different planetary atmospheres.

Neutral atmospheres and ionospheres can be affected by coupling to an external plasma, such as the solar wind or a magnetospheric plasma. Therefore, in addition to being modified by the solar photon flux they can be modified by the energy deposited by the incident plasma ions and electrons. This flux might be associated with the solar wind plasma or, for satellites orbiting in a planet's magnetosphere, a trapped, magnetospheric plasma. The energy range of the incident ions and electrons can be large, extending from eV's to many MeV's. When the energy deposition by the plasma can be calculated, then the subsequent modeling of the atmospheric processes, which is discussed in a number of associated reviews in this issue, is roughly independent of the exciting radiation. This is the case both for the quasi-thermal chemistry and the emission processes, but is also the case for the fate of the hot recoil particles produced by the incident ions or by exothermic chemistry. However, calculating the spatial distribution of the energy deposition versus depth into the atmosphere produced by an incident plasma is much more complex than is the calculation of the solar excitation profile, as discussed briefly below, but in detail by Ledvina et al. (2008). The complexity is due not only to the feedback processes that control the interaction of an ionized upper atmosphere with the ambient fields, but also because of the flux of locally produced pick-up ions. In this paper, the nature of the energy deposition processes by the incident plasma are described as is the fate of the hot recoils produced by exothermic chemistry and by knock-on collisions by the incident ions. This involves not only describing the molecular physics initiated by the incident radiations but also the transport process that occurs in the energized regions of the atmosphere.

2 Solar Photon and Photoelectron Energy Deposition

Most of the solar energy flux is in the visible and infrared regions of the spectrum, which are characterized by photons with wavelengths in the range $\sim 4000-50{,}000$ Å. The photons in the visible (4000−8000 Å) and near ultraviolet (NUV) ($\sim 2000-4000$ Å) region of the solar spectrum arise from the photosphere, which is characterized approximately by a blackbody spectrum with a temperature of ~ 6000 K. Solar photons with wavelengths in the far ultraviolet (FUV) ($\sim 1000-2000$ Å) and the extreme ultraviolet (EUV) ($\sim 100-1000$ Å), originate in the chromosphere and the transition region to the corona, where the temperatures are in the range 10^4-10^6 K. Soft X-rays ($\sim 10-100$ Å) arise from the solar corona. Some authors refer to an XUV region, which comprises the wavelength range of about from about 10 to 250 Å (e.g., Solomon et al. 2001). Harder X-rays ($1 < \lambda < 10$ Å), which arise from solar active regions, are absorbed in the mesosphere and the mesosphere/thermosphere boundary. Only about 2% of the solar energy flux is carried by photons in the ultraviolet and X-ray regions of the spectrum. The regions of the solar spectrum that are absorbed in the thermospheres and upper mesospheres of the planets are generally characterized by wavelengths less than 2000 Å.

2.1 Photoabsorption and Scattering of Visible Photons

In the visible portion of the spectrum, the photoabsorption cross sections for the major atmospheric species at high altitudes in solar system bodies are negligible. Exceptions to this generalization include some trace species, such as ozone, which absorbs weakly in the Chappuis bands from $\sim 4500-8500$ Å in the terrestrial and Martian atmospheres. Some hydrocarbon radicals, which may be found in small abundances in the middle atmospheres of the outer planets, theoretically may undergo photodissociation in the visible region to produce an energetic H atom, such as $C_2H_5 + h\nu \rightarrow C_2H_4 + H$, for which the threshold dissociation energy (DE) is 1.65 eV (7535 Å) (e.g., Gilbert et al. 1999) and the 2-propyl radical $C_3H_7 + h\nu \rightarrow C_3H_6 + H$ for which the DE is 1.536 eV (8071.9 Å) (e.g., Noller and Fischer 2007). Visible photons therefore either penetrate to the surfaces or are scattered by cloud and haze particles on all the planets and satellites that have significant atmospheres.

The surface of the Earth is only partially obscured by water and water-ice clouds, which cover about 40% of the planet. On Mars, visible photons are partly attenuated by highly temporally and spatially variable airborne dust (e.g., Kahn et al. 1992) and water-ice hazes, such as the those that surround the poles during winter, and those that form during the afternoon over the Tharsis and Elysium uplands (e.g., Jakosky and Haberle 1992; Zurek et al. 1992).

On Venus, Titan and Triton, layers of clouds and hazes scatter visible photons and prevent them from penetrating to the surface. On Venus, the multi-layered cloud deck, which is composed of mostly sulfuric acid particles, water ices, and chlorine-containing species, extends from about 45 to 65 km. In the lower cloud layer there is evidence for a phosphorus-containing species such as phosphoric acid (H_3PO_4). Haze layers form above and below the main cloud layers (e.g., Esposito et al. 1983; Prinn 1985; Chamberlain and Hunten 1987; Esposito et al. 1997; de Pater and Lissauer 2001).

The ubiquitous hazes on Titan are probably composed of C_2 and higher hydrocarbons and large nitriles. Nitriles are organic species containing a triple CN bond, such as HCN (hydrogen cyanide), HC_3N (cyanoacetylene), CH_3CN (methyl cyanide) or C_2N_2 (cyanogen). These species are formed by ionizing and dissociating interactions of ultraviolet photons or energetic electrons with the major constituents CH_4 and N_2, followed by a rich and complicated photochemistry. The Titan surface is completely obscured by yellow-orange haze particles that are probably composed of tholins, which are

nitrogen-rich organic compounds or polymers. The haze particles are believed to contain a solid organic core (e.g., Baines et al. 1995; Israel et al. 2005; Tomasko et al. 2005; Lavvas et al. 2008). The cold surface of Triton, the temperature of which is of the order of 40 K, is also obscured partly by hazes that are probably composed of condensed hydrocarbons, and partly by patchy clouds of condensed N_2 (e.g., Gurrola et al. 1992; Stevens et al. 1992; Yelle et al. 1995).

The middle atmospheres of Jupiter and Saturn are characterized by various aerosols, hazes and multiple cloud layers that scatter visible radiation and limit its penetration to the lower atmospheres (e.g., Atreya et al. 1999; Moses 2000; West et al. 2004; Kim et al. 2006). Although NH_3 is an important minor component of the lower atmospheres of these planets (e.g., (Taylor et al. 2004); de Pater and Massie 1985; de Pater and Lissauer 2001), ammonia and NH_4SH condense to form cloud layers in the tropospheres of Jupiter and on Saturn. At higher altitudes, in the stratospheres of these planets, hydrocarbon haze layers are also present (e.g., Moses 2000; Kim et al. 2006). In the colder atmospheres of Uranus and Neptune, photochemical hydrocarbon hazes and ices may form in the stratospheres (e.g., Moses et al. 1992), and methane ices probably form tropospheric clouds (e.g., Baines et al. 1995).

2.2 Absorption of Ultraviolet Photons

The major thermospheric species of the terrestrial planets with oxidizing atmospheres (Venus, Earth and Mars) include O_2, N_2, CO_2, and Ar, with small admixtures of He, H_2, and the photolysis products, O, N, NO, CO and H. CO_2 is the major species in the lower thermospheres of Mars and Venus, but is a minor species in the terrestrial thermosphere. Although CO_2 condenses onto the surface of Mars none of the major or minor species condenses in the thermospheres of the planets, which are heated by EUV and FUV radiation (e.g., Roble et al. 1987; Fox and Dalgarno 1979, 1981; Fox 1988; Fox et al. 1995).

In the reducing thermospheres of the outer planets (Jupiter, Saturn, Neptune and Uranus), H_2, He, H, CH_4 and its photolysis products, CH_3, CH_2, and CH, along with photochemically produced higher hydrocarbons, are the dominant constituents (Gladstone et al. 1996; Yelle and Miller 2002).

The atmospheres of Titan and Triton are composed mostly N_2 and are of intermediate oxidation state; the thermospheres also contain small amounts of CH_4, H_2, and small radical species formed by chemistry initiated by photon or energetic electron impact, such as N, C and H. The abundances of C_2H_2, C_2H_6, C_2H_4, higher hydrocarbons, and nitriles such as HCN and HC_3N, and CH_3CN are significant in the lower thermospheres and the middle atmospheres (e.g., Krasnopolsky et al. 1993; Krasnopolsky and Cruikshank 1995; Keller et al. 1992; Marten et al. 2002; Yelle et al. 2006).

The photoabsorption cross sections for the small molecules and atoms that make up planetary thermospheres maximize in the extreme ultraviolet (EUV), with values of $\sim 10^{-17}-10^{-15}\,\mathrm{cm}^2$, and optical depth unity is reached for column densities in the range $(1-100)\times 10^{15}\,\mathrm{cm}^{-2}$. Therefore, any solar system body with a substantial atmosphere has a thermosphere and an ionosphere.

We here limit our discussion to the effects of absorption of FUV, EUV and soft X-ray photons. We specifically ignore the effects of the absorption of solar near infrared photons, which, however, play an important role in heating the lower thermospheres of the planets (e.g., Bougher et al. 1990; López-Valverde et al. 1998; Roldán et al. 2000; Bougher et al. 2008).

The absorption of photons in the far UV, EUV, and soft X-ray regions of the spectrum may lead to dissociation, ionization, or, in some cases, fluorescence of thermospheric species. The rate of absorption of photons that are characterized by wavelength λ at altitude z, $q_\lambda^a(z)$, is given by

$$q_\lambda^a(z) = F_\lambda(z)\sigma_\lambda^a n(z) \tag{1}$$

where σ_λ^a is the absorption cross section, $n(z)$ is the local number density, $F_\lambda(z) = F_\lambda^\infty \exp(-\tau_\lambda(z))$ is the local solar photon flux, and F_λ^∞ is the photon flux at the top of the atmosphere. The optical depth in a plane parallel atmosphere at altitude z is $\tau_\lambda(z, \chi) = \int_z^\infty \sigma_\lambda^a n(z')\sec(\chi)dz'$, where χ is the solar zenith angle. It can be easily shown that the maximum absorption rate in such an atmosphere for solar zenith angle χ is found at the altitude at which $\tau_\lambda(\chi)$ is unity. In order to compute the total photoabsorption rate, (1) must of course be integrated over all wavelengths. In any realistic multi-constituent atmosphere, the rate of photoabsorption must also be summed over all major species.

The column density above an altitude z is defined as $N(z) = \int_z^\infty n(z')dz'$. Note that here we have denoted the local number density $n(z)$, and we have reserved $N(z)$ to indicate the column density. For an atmosphere in hydrostatic equilibrium, the variation of pressure P with altitude is given by

$$\frac{dP(z)}{dz} = -\rho(z)g(z) \tag{2}$$

where the $\rho(z)$ is the mass density and $g(z)$ is the acceleration of gravity.

In the following equations, most of the variables are altitude dependent, but for the purpose of compactness, we have suppressed the variable z. The pressure P at a given altitude is just the force (or weight) per unit area of the atmosphere above that altitude, which is simply given by $P = Nm_a g$. The pressure can also be expressed by the ideal gas law:

$$P = nkT = Nm_a g \tag{3}$$

where k is Boltzmann's constant. Combining the ideal gas law with the definition of $\rho = nm_a$, where m_a is the average mass of the atmospheric constituents, we can derive an expression for the mass density, $\rho = (Pm_a/kT)$. Substituting this expression into (2) and rearranging, we obtain

$$dP/P = \frac{-m_a g}{kT}dz = -1/H_p, \tag{4}$$

where the pressure scale height H_p is defined as kT/mg. Equation (4) can be integrated to give the barometric formula

$$P = P_0 \exp\left(-\int_{z_0}^{z} 1/H_p\right). \tag{5}$$

In this equation, the subscript 0 indicates an arbitrary reference level.

Equations (3) can be rearranged to give a simple expression for the vertical column density

$$N = n\frac{kT}{m_a g} = nH_p. \tag{6}$$

This rather general expression is valid if we assume that the acceleration of gravity and m_a are constant; these assumptions are valid over altitude ranges of the order of a scale height in

the mixed region of the atmosphere, that is, below the homopause. For $\chi \neq 0$, the altitude of unit optical depth occurs where the column density along the line of sight to the sun $N(\chi) = N(0)\sec(\chi)$ is the inverse of the absorption cross section, i.e., $N(\chi) = {\sigma_a}^{-1}$. The photon fluxes F_λ^∞ at the top of the atmosphere depend on the distance of the planet from the Sun at a given place in its orbit, solar activity (usually as measured by a suitable proxy), and the solar flux model that is used.

2.3 Solar Flux Models

Among the early versions of the solar spectra used in modeling are those of Hinteregger et al. (e.g., 1981), which were based on measurements of the EUVS experiment on the Atmosphere Explorer satellites. The measurements were normalized and extended outside the wavelength range of the satellite measurements, 142–1850 Å using data from rocket experiments (e.g., Heroux and Hinteregger 1978). Often the solar flux models are denoted by the last two digits of the year and the 3 digit ordinal day of year that they apply to, such as 74113, 76200 (which is also known as SC#21REFW, the successor to the F76REF), and 79050. The first two spectra pertain to low solar activities and the latter to high solar activity of solar cycle 21. In "Hinteregger-style" spectra, the solar fluxes are given at 1 Å resolution in the continua, and as delta functions at the central wavelength of the strong solar lines, for a total of more than 1800 wavelengths from 18 to 2000 Å. Sometimes larger spectral ranges are used, for a total of 37 intervals from 50 to 1050 Å (e.g., Torr et al. 1979). The Hinteregger spectra are also known as the SERF1 solar flux models (e.g., Tobiska 1991).

More recently, the solar fluxes that have been used in thermosphere/ionosphere modeling have been derived from the SOLAR 2000 (S2K) models of Tobiska (e.g., Tobiska 2004; Tobiska and Bouwer 2006). The S2K v2.2x spectra are normalized to the measurements from the Solar EUV Experiment (SEE) on the Thermosphere Ionosphere Mesosphere Energetics and Dynamics (TIMED) spacecraft. The SEE instrument has measured solar irradiances in the range 1 to 1940 Å in 10 Å intervals from 2002 to the present. (e.g., Woods et al. 2005; see also the instrument website at lasp.colorado.edu/see). Other commonly used models include the S2K v1.24 spectra, which are normalized to the data from the Student Nitric Oxide Explorer (SNOE) spacecraft (e.g., Bailey et al. 2000). The latter spectra yield larger peak electron densities that are in better agreement with the measured electron density profiles for Mars and Venus. In Fig. 1a, we present the photon fluxes of the S2K 2.22 model for day 76200 (low solar activity) from 18 to 2000 Å; in Fig. 1b, we show the ratio of the S2K 2.22 photon fluxes to those of the S2K v1.24 spectrum over the range 18 to 1100 Å.

2.4 Chapman Layer Theory

The interaction of photons with atmospheres was first described in a simple but insightful way by Chapman (1931a). The details of Chapman layer theory have been described in many textbooks (e.g., Rishbeth and Garriott 1969; Bauer 1973; Banks and Kockarts 1973; Schunk and Nagy 2000; Bauer and Lammer 2004), and will not be repeated here. Although a Chapman layer need not be an ion/electron layer, we will confine ourselves to a brief presentation of the salient features and most important equations for ionospheric ion and electron density profiles.

In Chapman layer theory for ions, the thermosphere is assumed to be composed of one molecular constituent, XY, which is ionized by the absorption of monochromatic solar photons

$$\mathrm{XY} + h\nu \rightarrow \mathrm{XY}^+ + \mathrm{e}. \tag{7}$$

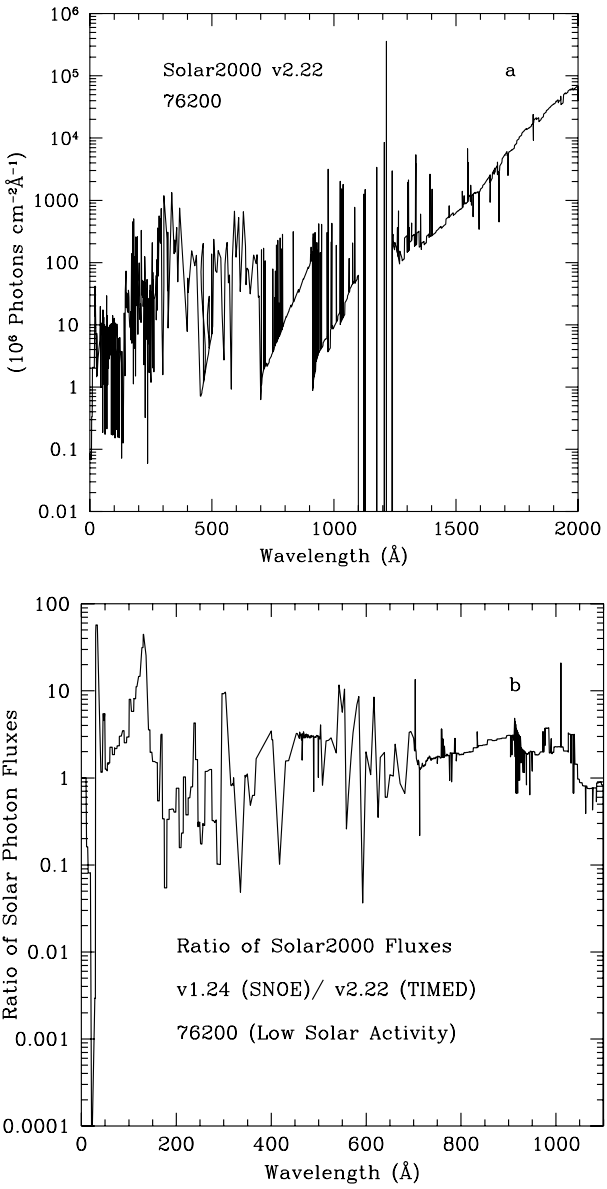

Fig. 1 (**a**) Photon fluxes from 18 to 2000 Å for the 76200 S2K v2.22 solar flux model of Tobiska (2004). (**b**) Ratio of S2K 2.22 v1.24 photon fluxes to the S2K 2.22 photon fluxes from 18 to 1100 Å

The ion XY^+ is destroyed locally by dissociative recombination with a rate coefficient α_{dr}:

$$XY^+ + e \rightarrow X + Y. \tag{8}$$

The production rate of XY^+ by photoionization is given by a general equation similar to that for photoabsorption above (see (1)):

$$q^i = F\sigma^i n_{XY}, \tag{9}$$

where n_{XY} is again the number density of the neutral molecule XY, and σ^i is the ionization cross section. The loss rate for dissociative recombination is given by $L = \alpha_{DR} n_i n_e$, where n_i is the ion density, which, because of charge neutrality, is equal to n_e, the electron density. In Chapman theory photochemical equilibrium (PCE) is assumed, which means that at steady-state, the photochemical production and loss rates are equal. The electron and ion densities are given by

$$n_e = n_i = \left[\frac{F \sigma^i n_{XY}}{\alpha_{dr}} \right]^{1/2}. \tag{10}$$

In Chapman theory the temperature T and mass of XY are assumed to be constant; furthermore, if the altitude dependence of the acceleration of gravity g is ignored, $H_p = kT/mg$ is a constant and the barometric formula (5) can be expressed in terms of the number density $n_{XY}(z) = n^0_{XY} \exp(-z/H)$, where n^0_{XY} is the number density at an arbitrary reference altitude, which may be defined as $z = 0$. Under these conditions the pressure and number density scale heights are equal. If the production rate of ions in a Chapman layer for solar zenith angle (χ) is given by (9), and the maximum ionization rate occurs at $z = 0$ where $\tau = 1$:

$$q^i_{\max,\chi} = \frac{F^\infty}{e} \frac{\sigma^i}{\sigma^a H \sec\chi} = \frac{q^i_{\max,0}}{\sec\chi}, \tag{11}$$

The ionization rate q^i_χ at altitude z can be expressed in terms of the maximum ionization rate for overhead sun as

$$q^i_\chi(z) = q^i_{\max,0} \exp\left[1 - \frac{z}{H} - \sec\chi\, e^{-z/H} \right]. \tag{12}$$

Combining (10) and (12), the ion density profile in Chapman theory for a plane parallel atmosphere is given by

$$n_{\rm i}(z) = \left[\frac{q^i(z)}{\alpha_{\rm dr}} \right]^{1/2} = \left[\frac{q^i_{\max,0}}{\alpha_{\rm dr}} \right]^{1/2} \exp\left[\frac{1}{2} - \frac{z}{2H} - \frac{1}{2} \sec\chi\, e^{-z/H} \right], \tag{13}$$

and the maximum ion or electron density as a function of solar zenith angle is then

$$n^i_{\max,\chi} = n^i_{\max,0} (\cos\chi)^{0.5}. \tag{14}$$

The mathematically elegant theory described above is confined to the plane parallel approximation, which becomes increasingly invalid as the terminator is approached. For near terminator region, the sphericity of the atmosphere must be taken into account. In these cases, $\sec\chi$ is often replaced by the Chapman Function, $Ch(x, \chi)$, where $x = R/H_n$, R is the distance from the center of the planet, and H_n is the (constant) neutral scale height. The Chapman Function, which is the ratio of the number density along the line of sight to the Sun in spherical geometry to the vertical column density, has been approximated by various combinations of analytical functions (e.g., Chapman 1931b; Rishbeth and Garriott 1969; Smith and Smith 1972; Bauer 1973). Huestis (2001) has reviewed the various approximations, and described a new analytical evaluation of the Chapman function that is accurate for a large range of χ and for small values of x. Since the advent of fast computers, however, the use of the Chapman function has become unnecessary.

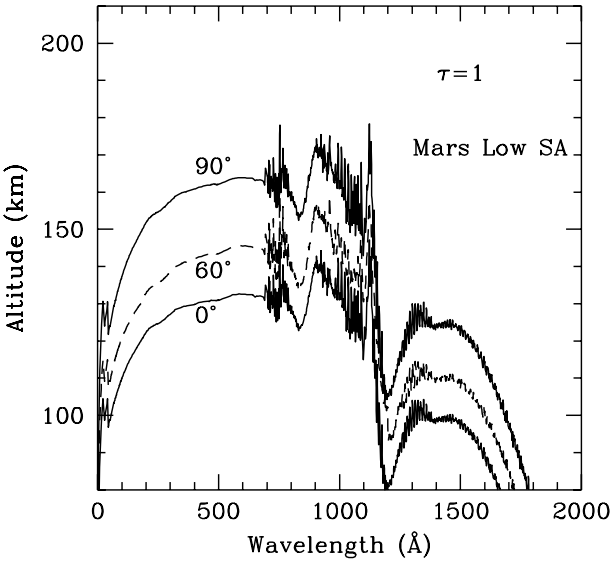

Fig. 2 Altitude of optical depth unity for a low solar activity model of Mars for 0, 60 and 90° SZA

It is fairly easy to compute the optical depth $\tau(\lambda, z, \chi)$ along the line of sight to the Sun in spherical geometry numerically, as described, for example by Rees (1989). For solar zenith angles χ less than 90°,

$$\tau(\lambda, z, \chi) = \sum_j \int_z^\infty n_j(z')\sigma_j^a(\lambda)\left[1 - \left(\frac{R+z}{R+z'}\right)^2 \sin^2\chi\right]^{-0.5} dz', \tag{15}$$

where R is the planetary radius, and the sum over species j is shown explicitly. For χ greater than 90°, the optical depth can be computed as

$$\tau(\lambda, z, \chi) = \sum_j \left\{ 2\int_{z_s}^\infty n_j(z')\sigma_j^a(\lambda)\left[1 - \left(\frac{R+z_s}{R+z'}\right)^2 \sin^2 90^\circ\right]^{-0.5} dz' \right.$$
$$\left. - \int_z^\infty n_j(z')\sigma_j^a(\lambda)\left[1 - \left(\frac{R+z}{R+z'}\right)^2 \sin^2\chi\right]^{-0.5} dz' \right\} \tag{16}$$

where z_s is the tangent altitude. It is of course unnecessary to include the $\sin^2 90^o = 1$ factor explicitly in the first term on the right of (16), but we include it here in order to clarify the origin of the formula for the optical depth as twice the total horizontal optical depth along the line of sight to the sun minus that beyond the solar zenith angle χ.

Figure 2 shows optical depth unity as a function of wavelength from the soft X-ray region to the mid FUV region for a low solar activity model of Mars for solar zenith angles 0, 60 and 90°. There is a small increase in the penetration depth as the solar zenith angle increases from 0 to 60°, but a somewhat larger increase occurs from 60 to 90° SZA.

Because of the simplifying assumptions built into the Chapman layer theory, there is no reason to believe that real ionospheric profiles are even quasi-Chapman. Although thermospheric temperatures approach a constant value, T_∞, at high altitudes in stationary atmospheres, thermospheric temperatures increase rapidly near and above the ion peak, where much of the solar energy is deposited.

Table 1 Ionization potentials (I_P) of Some Species of relevance to Planetary Atmospheres[a]. Units are eV

High I_P		Medium I_P		Ionized by Ly α	
Species	I_P	Species	I_P	Species	I_P
He	24.59	H_2O	12.61	C_4H_2	10.18
Ne	21.56	CH_4	12.51	NH_3	10.16
Ar	15.76	SO_2	12.32	CH_3	9.84
N_2	15.58	CH_3CN	12.194	C_3H_6	9.73
H_2	15.43	O_2	12.07	NO	9.264
N	14.53	HC_3N	11.64	C_6H_6	9.246
CO	14.01	C_2H_6	11.52	Si	8.152
CO_2	13.77	C_2H_2	11.40	C_2H_5	8.13
O	13.618	C	11.26	HCO	8.10
H	13.598	C_3H_8	10.95	C_3H_7	8.09
HCN	13.60	CH	10.64	Fe	7.87
OH	13.00	C_2H_4	10.51	Mg	7.65
		H_2S	10.45	trans-HCNH	7.0[b]
		CH_2	10.4	cis-HCNH	6.8[b]
		S	10.35	Ca	6.11
				Na	5.139

[a]Computed with data from Lias et al. (1988), except as noted

[b]From Nesbitt et al. (1991)

Thermospheres also have multiple neutral constituents, and ionospheres are composed of many ions; they are not in PCE at high altitudes. In fact, the largest peaks on the Earth and outer planets are composed of atomic ions O^+ and H^+, respectively, and are F_2 peaks (e.g., Banks and Kockarts 1973; Hinson et al. 1998; Waite and Cravens 1987). F_2 peaks are formed where the time constant for loss by chemical reactions, $\tau_c = 1/\mathcal{L}$, where $\mathcal{L} = L/n$ is the specific loss rate, is equal to the time constant for diffusion, $\tau_d = H^2/D$, where D is the ambipolar diffusion coefficient. Thus PCE breaks down as the F_2 peaks are approached from below.

In addition, the ionizing fluxes are not monochromatic, but cover a range from the ionization potentials of the species to the soft X-ray region of the solar spectrum. Ionization potentials of the common atmospheric species in the atmospheres of the planets are shown in Table 1. The photoionization cross sections, $\sigma^i(\lambda, j)$ and the photoabsorption cross sections $\sigma^a(\lambda, j)$ are functions of wavelength λ and are species dependent. The dissociative recombination coefficient α_{dr} depends on the identity of the ion and has a dependence on the electron temperature that is usually expressed as $(300/T_e)^b$. In this formula, the exponent b has a theoretical value of 0.5, but is found experimentally to be in the range 0.2−0.7, and may itself be temperature dependent. Most important, ionization by solar photons is supplemented by that of photoelectrons, which in general deposit their maximum energy below that of photons.

On the topsides, the ion and electron density profiles are determined to varying extents by the electron (T_e) and ion (T_i) temperatures which are equal to the neutral temperatures only in the lower ionosphere where collision rates between neutrals, ions and electrons are high. The plasma temperatures are larger than T_n at higher altitudes. Some examples of neutral, ion and electron temperature profiles are given in Fig. 3 of Witasse et al. (2008).

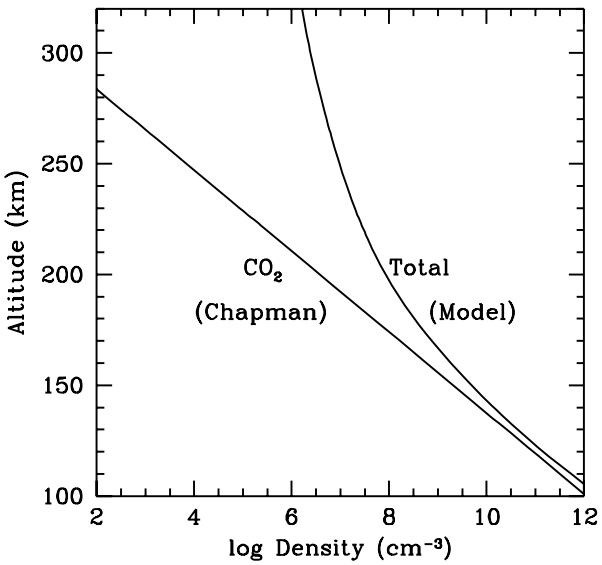

Fig. 3 Altitude profiles of total neutral densities for models based on Chapman profiles and a realistic profile from a model of Mars. The Chapman neutral model profile consists of pure CO_2, while the realistic model profile is made up of 12 neutral species. It is clear that the scale height increases with altitude in the realistic model. This is a result of increasing neutral temperatures, and increased abundances of lighter species

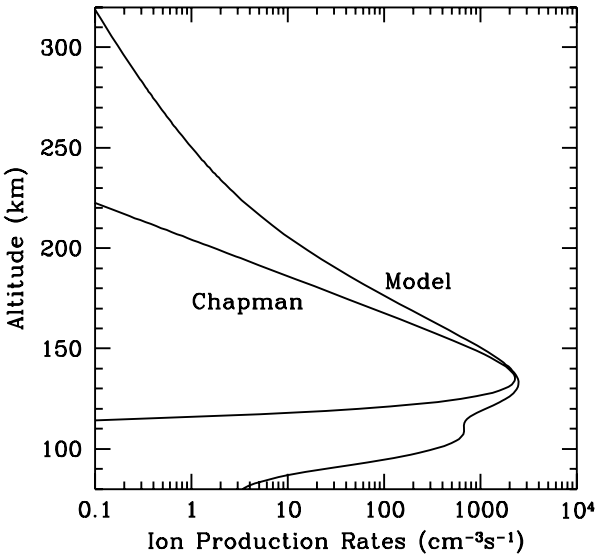

Fig. 4 Ion production rates for the models shown in Fig. 3. Neither the topside nor the bottomsides of the Chapman profiles fit the model profiles

In order to compare Chapman profiles with detailed, realistic numerical models, we have constructed a 60° SZA low solar activity model of the Martian thermosphere/ionosphere similar to those of Fox (2004). In order to fit the Chapman profile, we have determined the CO_2 number density profile for which the ionospheric peak magnitude and altitude reproduce the F_1 peak of the realistic model. This CO_2 profile is compared to the total neutral number density profile of the realistic model in Fig. 3. The resulting ionization profile from 100 to 320 km for the realistic model is presented in Fig. 4 where it is compared with that of the Chapman layer production profile. It is obvious that the realistic ionization profile does not fit the Chapman model at either low or high altitudes. At high altitudes the temperature

increases above that at the peak, and the abundance of light atoms increase. This results in an increasing neutral scale height above the peak, rather than a constant scale height as required by Chapman theory.

Photoionization of the various atmospheric species by EUV photons occurs over a broad wavelength range, which in turn causes broadening of the upper F_1 electron density peak. The major mechanism for production of ions in this region is absorption of EUV photons. In fact, this is how we define the F_1 peak here (Banks and Kockarts 1973; Bauer 1973; Bauer and Lammer 2004). Other workers have defined it differently. The photoelectrons produced near the F_1 peak may cause further ionization. The maximum in the ion production rate profile for photoelectrons is slightly below that of photons in the F_1 region. Solar soft X-rays penetrate to lower altitudes in the thermosphere, and produce very high energy photoelectrons. These photoelectrons may produce multiple ionizations at altitudes below the lower E-region peak in the photoionization profile. For example, in a high solar activity model of the Martian ionosphere, the average energy of the photoelectrons produced near the F_1 peak at 135 km is 25.1 eV, and that near the E peak at 117 km is 161 eV.

In fact, ionization at the lower (E-region) peak is caused mainly by impact of photoelectrons and secondary electrons:

$$CO_2 + e^* \rightarrow CO_2^+ + e^* + e, \tag{17a}$$

$$CO_2 + e^* \rightarrow CO^+ + O + e^* + e, \tag{17b}$$

$$CO_2 + e^* \rightarrow O^+ + CO + e^* + e, \tag{17c}$$

where the asterisk denotes an electron with enough energy to potentially produce further ionization. Equations (17b) and (17c) illustrate dissociative ionization of CO_2, which is the main source of the fragment ions O^+ and CO^+ ions at the E-region peak. A comparison of the sources of ionization caused by photons and photoelectrons is shown in Figs. 5a and 5b.

The model electron density profile between the altitudes of 100 and 320 km is compared to that of a Chapman layer in Fig. 6. It is easily seen that the model profile and the Chapman layer are very different both above and below the peak. The Chapman layer is characterized by a constant scale height above the peak, and the electron densities fall off rapidly below the peak. The model electron densities are, however, larger and are characterized by scale heights that vary above the peak. Above about 180 km the scale height increases rapidly, so that near the 300 km, the difference in densities is nearly 3 orders of magnitude. The ion number density scale height H_n^i differs from the plasma pressure scale height $H_p^i = kT_p/(m^i g)$, where m^i is the ion mass and $T_p = T_i + T_e$ is the plasma temperature according to the equation

$$\frac{1}{H_n^i} = \frac{1}{H_p^i} + \frac{1}{T_p}\frac{dT_p}{dz}. \tag{18}$$

At high altitudes where the plasma temperatures increase rapidly in the model, the second term on the right becomes larger than the first, and all the ions are characterized by the same scale height. In addition, PCE breaks down for O_2^+ in the Mars models above an altitude of about ~ 184 km at low solar activity and near ~ 216 km at high solar activity.

As Fig. 6 illustrates, in the region below the F_1 peak, where the Martian ion production rate is dominated by absorption of soft X-rays and the concomitant ionization by high energy photoelectrons and secondary electrons, the model densities are much larger than those of the single Chapman layer model, in which the ionizing photons are monochromatic. The total electron content (TEC) of the model is $\sim 4.9 \times 10^{11}$ cm^{-2}, whereas the TEC for the Chapman profile is 2.7×10^{11} cm^{-2}, which is smaller by almost a factor of two.

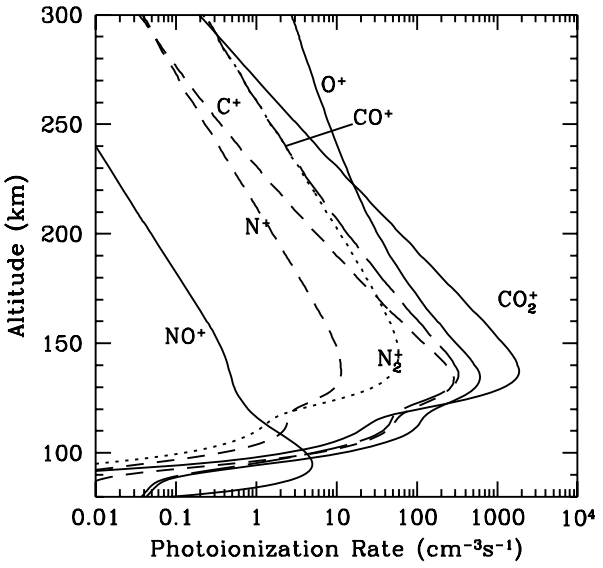

(a)

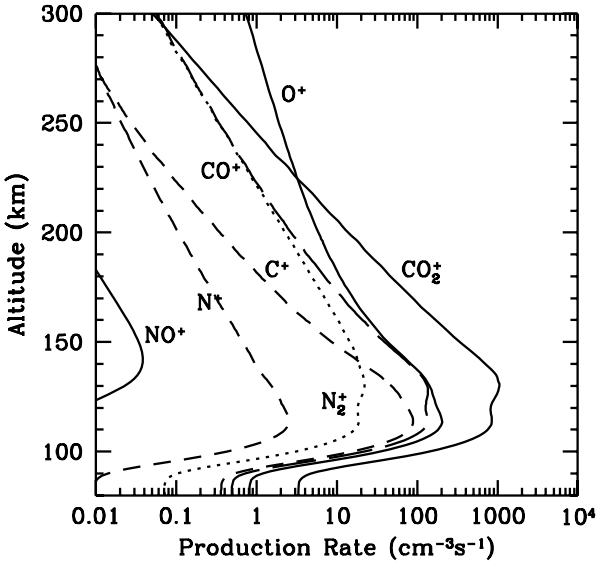

(b)

Fig. 5 Computed ionization rate profiles from 80 to 300 km for 7 ions for a high solar activity 60° SZA model of Mars. (**a**) Production rates by photoionization. (**b**) Production rates by energetic photoelectron and secondary electron impact. Near the F_1 peak, the ionization is mostly by EUV photons. Near the E-region peak, however, ionization by very energetic photoelectrons and further electrons produced by electron impact ionization dominate

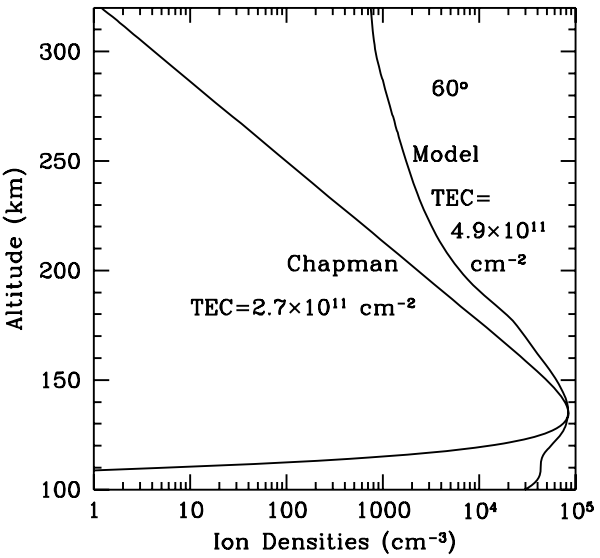

Fig. 6 Total ion or electron density profiles for the Chapman model and the realistic 60° SZA Mars models. These densities correspond to the neutral density profiles and production rates in Figs. 3 and 4. The total electron contents (TEC) are compared

2.5 Photodissociation

Photodissociation is a major source of thermal, and translationally or electronically excited atoms and small fragments in the thermospheres and mesospheres of the planets. Photodissociation can be represented as

$$\mathrm{XY} + \mathrm{h}\nu \rightarrow \mathrm{X} + \mathrm{Y}, \tag{19}$$

where XY is a molecule, X and Y are fragments; the rate of dissociation, q^d, can theoretically be determined similarly to that of ionization (see (9))

$$q_\lambda^d = F_\lambda \sigma_\lambda^d n_{XY}, \tag{20}$$

where σ_λ^d is the wavelength dependent photodissociation cross section, and n_{XY} is the number density of the molecule. As always, q^d, F and n_{XY} are functions of altitude. To a first approximation, the photoabsorption cross section is the sum of the photoionization and photodissociation cross sections. To obtain the total photodissociation rate, q_λ^d must be summed over wavelengths in the solar spectrum from the photodissociation threshold to the point where the photodissociation cross section is zero, that is, where photoabsorption cross section is equal to the ionization cross section. For simple molecules, such as H_2, N_2, O_2, CO, and CO_2, that wavelength is the range ~600–750 Å (e.g., Berkowitz 2002). Model calculations of photodissociation rates in atmospheres may appear to be simple, but in practice, they are complicated by several factors. Measured photoionization cross sections in the continuum shortward of about 600 Å, where photodissociation does not compete with ionization are fairly accurate. Immediately shortward of the photoionization threshold, however, the photoabsorption cross sections usually are highly structured. In this region the photodissociation cross sections are calculated as the difference between the photoabsorption cross sections and the photoionization cross sections, which may be the difference between two large numbers. In addition, if the photoionization and photoabsorption cross sections are not

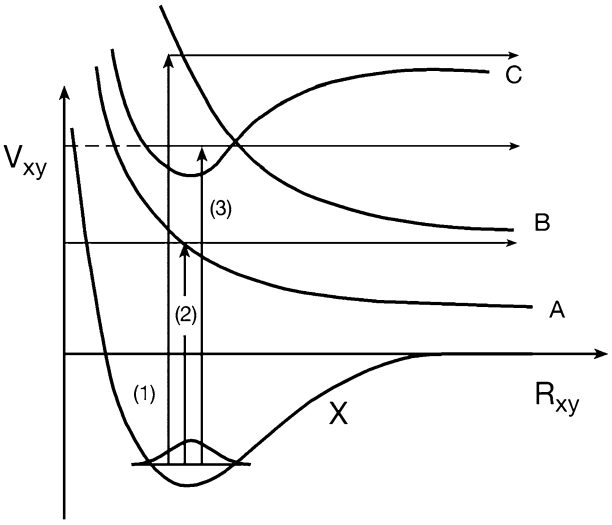

Fig. 7 Schematic representation of the three major mechanisms for photodissociation. (*1*) Excitation to the continuum of bound state (C) (*2*) Excitation to the purely repulsive state (A). Discrete excitation to a bound state (C) that is predissociated by a radiationless transition to the repulsive state (B)

adopted from a single source, there is a large potential for error in the computation of the photodissociation cross sections.

Longward of the photoionization threshold, the photoabsorption cross sections are usually taken to be equal to the photodissociation cross sections. In principle, the absorption of some photons may lead directly to fluorescence, but the fraction is generally small. For example, weak visible fluorescence in the wavelength range of 5500–7500 Å has been detected in the photoabsorption of O_2 at 1162 Å by Lee and Nee (2000), and provisionally attributed to the O_2 $D^3\Sigma_u^+(v' = 6) \rightarrow C^3\Pi_g(v'')$ transition.

Photodissociation can proceed via three possible mechanisms, which are illustrated schematically in Fig. 7. Absorption of a photon may excite a molecule into the continuum of an excited state (process 1), or to a purely repulsive state (process 2). The photodissociation cross sections for both of these processes are fairly smooth as a function of wavelength, and the photodissociation rates may usually be modeled with relatively low resolution cross sections and solar fluxes, of the order of 0.5–1 Å. Alternatively, photons may be absorbed into discrete excited states of the molecule, followed by predissociation (process 3). In order to model the rates of photodissociation proceeding via this mechanism, the individual bands must be resolved and the predissociation probabilities must be known. The photoabsorption rate must be modeled using very high resolution (of the order of 10^{-3} Å) photodissociation cross sections and a similarly high resolution solar spectrum. In addition, the photoabsorption cross sections are usually temperature dependent, and therefore the cross sections must be measured and calculations carried out at temperatures relevant to the part of the atmosphere where the absorption takes place.

We will illustrate these processes by describing the photoabsorption characteristics of some atmospherically important molecules. In order to illustrate the wealth of possible processes, we will focus on the details for O_2, which, because of its importance in the terrestrial atmosphere, has been the subject of many investigations. Photoabsorption by other relevant planetary thermospheric molecules will be discussed briefly.

2.6 Photoabsorption of O_2

In the wavelength region between the O_2 photoabsorption threshold at 2424 Å (5.11 eV) and about 2050 Å, most to the photodissociation is via the dipole forbidden absorption directly into the continuum of the $A^3\Sigma_u^+$ state (process 1). This is the upper state of the Herzberg I system:

$$O_2(X^3\Sigma_g^-) + h\nu \rightarrow O_2(A^3\Sigma_u^+) \tag{21a}$$

$$\rightarrow O(^3P) + O(^3P). \tag{21b}$$

Excitation into the continua of the O_2 ($A'^3\Delta_u$) state (the upper state of the Herzberg III band system) and the O_2 ($c^1\Sigma_u^-$) state (the upper state of the Herzberg II band system) also contribute to a lesser extent (e.g., Saxon and Slanger 1986). From 2050 to 2400 Å the cross sections decrease from about 7×10^{-24} to 1×10^{-24} cm^2 (e.g., Yoshino et al. 1988). Because the cross sections are very small, absorption by O_2 in the Herzberg continuum takes place in the terrestrial stratosphere where it competes with absorption by O_3. In the wavelength region between 192 and 205 nm, the absorption into the Herzberg continuum is much less efficient than that into the first Schumann-Runge (S-R) bands (e.g., Coquert et al. 1990; Yoshino et al. 1992).

Photoabsorption into the discrete states of the S-R band system of O_2 followed by predissociation dominates the absorption in the 1750–2050 Å range (process 3). The S-R bands arise from the dipole allowed photoabsorption process into discrete levels of the O_2 ($B^3\Sigma_u^-; v'$) state, followed by predissociation via a radiationless transfer to the repulsive $1^1\Pi_u$, $1^3\Pi_u$, $^5\Pi_u$, or $2^3\Sigma_u^+$ states:

$$O_2(X^3\Sigma_g^-; v'') + h\nu \rightarrow O_2(B^3\Sigma_u^-; v') \rightarrow O(^3P) + O(^3P) \tag{22}$$

(e.g., Julienne et al. 1997; Allison et al. 1986; Lin et al. 1996; Balakrishnan et al. 2000). As shown above, the product O atoms are in the ground ^3P states. Since the absorption cross sections in the region of the S-R bands vary greatly over wavelengths intervals of $\sim 10^{-4}$ nm, the cross sections must be measured with high resolution (e.g., Yoshino et al. 1984; Cheung et al. 1996; Matsui et al. 2003). High resolution absorption cross sections in the O_2 S-R Bands can be found on the CFA website (cfa-www.harvard.edu/amp/ampdata). Because the cross sections in the Schumann-Runge bands are of the order of $10^{-21}-10^{-19}$ cm^2, photons in this region of the absorption spectrum penetrate into the terrestrial mesosphere and stratosphere, where their photoabsorption is the principal O_2 dissociation process. They do not, however, affect the terrestrial thermosphere. The thermospheres of Mars and Venus do not contain enough O_2 to make photodissociation of O_2 an important as a source of O atoms.

Photoabsorption by O_2 in the wavelength range (130–175 nm) is mostly by direct absorption into the continuum of the $B^3\Sigma_u^-$ state, the S-R continuum (process 1):

$$O_2(X^3\Sigma_g^-; v'') + h\nu \rightarrow O_2(B^3\Sigma_u^-) \rightarrow O(^3P) + O(^1D). \tag{23}$$

The maximum cross section at 295 K is about 1.44×10^{-18} cm^2 near 1400 Å (e.g., Yoshino et al. 2005), and the products of this dissociation process are mostly $O(^3P) + O(^1D)$. Absorption of solar radiation by O_2 in the S-R continuum is the main source of atomic O in the terrestrial thermosphere.

Direct absorption from the ground state of O_2 to the $1^3\Pi_u$ state of O_2 is an approximate example of absorption into an excited state that has no bound state (process 2). Except for a

shallow minimum that is found in the 1.05–1.27 Å region, the potential curve is mostly repulsive (e.g., Allison et al. 1982). The photoabsorption cross sections into that state are small and smoothly varying at long wavelengths, but exhibit a sharp increase near 1358 Å, with considerable structure shortward of that wavelength (e.g., Allison et al. 1986; Balakrishnan et al. 2000).

In the wavelength range 1030 to 1300 Å, photodissociation of O_2 takes place via dipole allowed excitation of the $O_2(X^3\Sigma_g^-)$ ground state to discrete Rydberg states, such as the E, $E'^3\Sigma_u^-$ and the F, $F'^3\Pi_u$ states, which are strongly predissociated (process 3). This effect leads to highly structured cross sections, and an accidental, but important minimum appears at Lyman alpha (1216 Å). This is the "window" that allows penetration of solar Lyman alpha photons to low altitudes in the terrestrial atmosphere (e.g., Lee and Nee 2000, 2001). La Coursiere et al. (1999) have computed the relative yields of $O(^3P) + O(^3P)$ and $O(^3P) + O(^1D)$ over the solar Lyman alpha line, and have found that the $O(^1D)$ yield is about 0.58. Most of the rest of the yield in this region is to the products $O(^3P) + O(^3P)$. Only a small fraction of the dissociation produces $O(^3P) + O(^1S)$, with an upper limit less than 0.02.

Since the ionization potential of O_2 is 12.07 eV, photons shortward of 1027 Å can ionize or dissociate O_2. Jones et al. (1996) have shown that photons in the wavelength range 750 to 850 Å can excite O_2 to the I, I' and I'' Rydberg states that converge to the $O_2^+(a^4\Pi_u)$ state. In this wavelength range predissociation competes with autoionization, but, in general, predissociation is more important. Carlson (1974) has shown that absorption into these Rydberg states leads to production of one ground state $O(^3P)$ atom plus one excited state $O(^3S^o)$, which radiates to the ground state leading to the OI triplet at 1302, 1304, and 1306 Å.

2.7 Photodissociation of CO

Photodissociation of CO is important as a source of C on Venus and Mars. In the wavelength region 885 to threshold at 1118 Å, the photodissociation of CO takes place via discrete absorptions to a number of predissociating states (e.g., van Dishoeck and Black 1988). The line spacings in some of the bands are of the order of 10^{-4} Å. Fox and Black (1989) constructed high resolution cross sections for excitation to in six bands in the range 885–912 Å, and 33 bands considered by Black and van Dishoeck (1987) in the range 912–1118 Å, for a total of 39 bands to several electronic states. Fox and Black combined the computed high resolution cross sections with a model high resolution solar flux spectrum, which included measured or estimated lineshapes for the strong solar lines in this region of the spectrum. The photodissociation rates for the various bands in the Venus thermosphere were computed, and the total photodissociation rate was found to be smaller by a factor of two than those computed using the low resolution cross sections. The correction was small because CO is not the primary absorber in this region of the spectrum in the Venus atmosphere.

More recent measurements of high resolution photoabsorption cross sections for CO have been carried out for the wavelength regions 967–988 Å, and 925–974 Å by Stark et al. (1993) and Yoshino et al. (1995), respectively.

2.8 Photodissociation of N_2

Photodissociation of N_2 is potentially important for production of translationally and electronically excited N atoms in the planetary thermospheres. Low resolution cross sections for photoabsorption and photoionization of N_2 from 1 Å to the experimental threshold at 1021 Å (12.14 eV) are shown in Fig. 8. Photodissociation of N_2 in the region longward of the IP at 796 Å (15.58 eV) to 1021 Å takes place via line absorptions into discrete valence and

Rydberg states in the singlet manifold, which may decay by emission or preferably by predissociation (e.g., Helm and Cosby 1989). Although the energetic threshold for production of two ground state N atoms:

$$N_2 + h\nu \rightarrow N(^4S) + N(^4S) \tag{24a}$$

is 1270 Å (9.76 eV), the photodissociation cross sections longward of 1021 Å ($E <$ 12.14 eV) are found to be negligible. The possible channels for photodissociation of N_2 thus include

$$N_2 + h\nu(E > 12.14\text{ eV}) \rightarrow N(^4S) + N(^2D), \tag{24b}$$

$$N_2 + h\nu(E > 13.34\text{ eV}) \rightarrow N(^4S) + N(^2P), \tag{24c}$$

and

$$N_2 + h\nu(E > 14.52\text{ eV}) \rightarrow N(^2D) + N(^2D). \tag{24d}$$

For photon energies smaller than 14.52 eV, the dissociation produces one ground state and one excited state N atom. At energies larger than 14.52 eV (wavelengths shortward of 854 Å), in addition to line absorptions, there may also be some photodissociation directly into the continua of singlet *ungerade* repulsive states that result in the production of channel (24d) above (Michels 1981; Walter et al. 1993). Shortward of the ionization threshold at 796 Å ($E > 15.58$ eV) the photoabsorption cross sections are highly structured, and autoionization competes with predissociation. Photodissociations via the channels

$$N_2 + h\nu(E > 15.7\text{ eV}) \rightarrow N(^2D) + N(^2P) \tag{24e}$$

$$N_2 + h\nu(E > 16.9\text{ eV}) \rightarrow N(^2P) + N(^2P) \tag{24f}$$

are also possible, although the photoabsorption and photodissociation cross sections are difficult to measure in this spectral region (G. Stark, private communication, 2008).

In the highly structured regions of the N_2 photoabsorption spectrum, ultrahigh resolution cross sections and predissociation probabilities are required in order to quantitatively model the production of N atoms. Cross sections with resolutions of the order of $\sim 6 \times 10^{-3}$ Å are currently being measured by, for example, Stark et al. (2005, and references therein) and

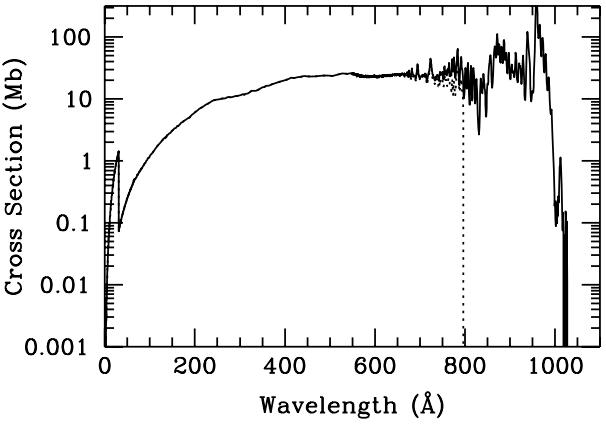

Fig. 8 Low resolution N_2 photoabsorption cross sections (*solid curve*). The photoionization cross sections are represented by the dotted curve. The experimental threshold for photodissociation is about 1021 Å (12.14 eV). In the highly structured region shortward of the ionization threshold at 796 Å predissociation and autoionization compete. Below about 650 Å the photoabsorption and photoionization cross sections are equal

Sprengers et al. (2005, and references therein). Lewis et al. (2005, and references therein) have computed predissociation lifetimes. Calculations carried out with lower resolution cross sections and low resolution solar fluxes can be considered to be accurate to a factor of only a few.

In addition, branching ratios to the various possible channels (24b–24f) must be known over the entire range of photodissociation. These data are not available, except for some information at energies less than 14.52 eV (see Fox 2007 for a review of this subject). Although progress is being made in determining high resolution cross sections and product yields of N_2, not enough information is currently available to accurately compute the production rates of various states of N atoms or the total photodissociation rate of N_2 in thermospheres/ionospheres of the earth, Venus, Mars, Titan or Triton.

2.9 Photodissociation of CO_2

The photoabsorption cross sections of CO_2 are also highly structured. Temperature dependent cross sections have been measured by Stark et al. (2007) from 1061 to 1187 Å with a moderate resolution of 0.05–0.1 Å. The values of the cross sections range from 5×10^{-16} to 2×10^{-20} cm^2 at 195 K, and thus photons in this region of the spectrum are absorbed over a wide altitude range in the atmospheres of Mars and Venus. In the wavelength region 1187 to 1755 Å, the CO_2 photoabsorption cross sections exhibit considerable structure. Photoabsorption cross sections in the 1178.08 to 1633.99 Å range have been measured by Yoshino et al. (1996) at moderate (~ 0.05 Å) resolution, and are available on the CFA website referenced above. Anbar et al. (1993) showed that the use of moderate resolution temperature dependent cross sections in the 1225 to 1970 Å region changed the CO_2 photolysis rates in the Martian lower atmosphere by about 33%, and those of H_2O by 950% as compared to those arising from the use of cross sections averaged over 50 Å bins.

2.10 Photodissociation of H_2

Dissociation of H_2 has a thermodynamic threshold of 4.48 eV (2769 Å), but the photoabsorption cross sections longward of 1116 Å are negligible. Photodissociation in the wavelength region 845–1116 Å proceeds largely by dipole-allowed absorption from the ground $X^1\Sigma_g^+(v'')$ state into discrete states, including $B^1\Sigma_u^+(v')$, $C^1\Pi_u(v')$, $B'^1\Sigma_u^+(v')$, and $D^1\Pi_u(v')$, which may then radiate either to the discrete levels of the ground state, producing emission, or to the continuum of the ground state, producing dissociation to form two H(1s) atoms (e.g., Dalgarno et al. 1970; Abgrall et al. 1997). The $B^1\Sigma_u^+(v')$ and $C^1\Pi_u(v')$ states are the upper states of the Lyman and Werner band systems, respectively, of H_2. Black and van Dishoeck (1987) have investigated these processes as they relate to the interstellar medium, where only radiation longward of the H ionization threshold of 912 Å is important. They found that about 10–15% of the initial line absorptions fluoresce to the continuum of the $X^1\Sigma_g^+(v'')$ state.

Except for a small contribution from predissociation of the $D^1\Pi_u$; v' state for $v \geq 3$ (e.g, Mentall and Gentieu 1970), these excited states are not predissociated in the usual sense because no suitable crossings to repulsive states are available. The lowest purely repulsive state of H_2 is the $b^3\Sigma_u^+$ state (Herzberg 1950), which, because of dipole selection rules, cannot be significantly populated by photoabsorption. Shortward of 845 Å, direct absorption into the continua of the $B^1\Sigma_u^+$, $C^1\Pi_u$, $B'^1\Sigma_u^+$, and $D^1\Pi_u$ states dominates the photodissociation. The cross sections for these processes are substantial, and the products of dissociation are one H(1s) atom and one H(2s, 2p) (e.g., Glass-Maujean 1986).

Autoionization of H_2 begins to compete with dissociation shortward of the ionization threshold at 803 Å, and the cross sections exhibit complicated structure in this region, which has not been fully analyzed (e.g., Yan et al. 1998). For example, dissociation of the $B''\bar{B}^1\Sigma_g^+$ double-welled state proceeds by radiation to the continuum of the $B'^1\Sigma_u^+; v'$ state, with a rate of the order of 5×10^{10} s^{-1} (e.g, Glass-Maujean et al. 2007).

In environments in which H_2 is the major absorber, such as the thermosphere of Jupiter, radiation shortward of 912 Å is important. Significant effects of discrete absorption on the atmospheric absorption profiles are predicted. Kim and Fox (1991, 1994) used the compilations of oscillator strengths, transition probabilities, and fluorescent dissociation fractions of Black and van Dishoeck (1987) and some additional lines provided by J. H. Black (private communication, 1990) shortward of 912 Å to construct high resolution H_2 photoabsorption cross sections. Kim and Fox combined these cross sections with a similarly high resolution solar flux spectrum, and found that, in the Jovian atmosphere, solar radiation in the line centers penetrates to only 420 km above the ammonia cloud tops, but in the wings of the photoabsorption lines, two strong solar lines, CIII at 977.02 Å and OVI at 1031.91 Å, and about 30% of the continuum, penetrate 100 km further to below the methane homopause, where the production of a layer of hydrocarbon ions was predicted.

2.11 Photodissociation of Hydrocarbons

The photoabsorption cross sections for methane fall off rapidly longward of about 1450 Å (e.g., Lee and Chiang 1983), but other hydrocarbons expected to be found below the methane homopauses of the giant planets, such as acetylene, ethane, and ethylene, absorb at longer wavelengths. The cross sections are found, however, to be highly structured and temperature dependent. Photoabsorption cross sections for acetylene have been measured, for example, by Smith et al. (1991) at a resolution of $\sim 0.1-0.5$ Å. Temperature dependent cross sections for ethylene have recently been measured with a resolution of 0.6 Å by Wu et al. (2004). For other hydrocarbons, the reader is referred to the *science-softCon UV/Vis Spectra Data Base*, in which the available data on photoabsorption of hydrocarbons and other molecules of atmospheric interest are summarized and presented (Noelle et al. 2007; see also Huestis et al. 2008).

2.12 Heating by Absorption of Solar Photons and Heating Efficiencies

The heating efficiency is usually defined as the fraction of solar energy absorbed that is deposited locally as heat. Solar energy is transformed into heat in photodissociation and photoelectron-impact dissociation of molecules, and in exothermic reactions, including ion-molecule reactions, neutral-neutral reactions, and dissociative recombination of ions with electrons. Quenching (or collisional deactivation) of metastable ions, such as $O^+(^2D)$, or neutrals, such as $O(^1D)$ or $N(^2D)$, is a particularly important class of reactions that lead to heating. A major uncertainty in modeling heating efficiencies is determining the fraction, f_v, of the exothermicities in these processes that appears as vibrational excitation of molecular products. Vibrational excitation usually leads to cooling either by direct radiation to space for heteronuclear diatomics or polyatomics, or by vibrational energy transfer from homonuclear diatomics to heteronuclear species, and subsequent radiation. By contrast rotational and translationally excited products are thermalized rapidly.

In photodissociation, the amount of energy that appears as kinetic energy is the difference between the energy of the photon and the dissociation energy (which may include some electronic excitation of the fragments). The energy that appears as vibrational excitation in

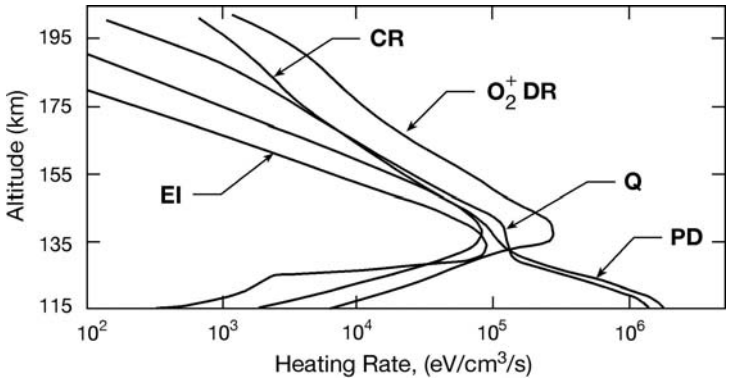

Fig. 9 Altitude profiles of computed heating rates in the Venus thermosphere. The *curve labeled CR* represents the heating rate due to exothermic chemical reactions; the *curve labeled* O_2^+ *DR* is that due to dissociative recombination of O_2^+; the *curve labeled Q* represents the heating due to quenching reactions of metastable species; the *curve labeled PD* is the heating rate due to photodissociation; the *curve labeled EI* is that due to electron impact processes. Adapted from Fox (1988)

photodissociation is found to be small, of the order of 25%. A half-collision model suggests that this fraction is particularly small if one of the fragments is light, such as H or H_2. Vibrational excitation fractions of 10–15% are indicated for this case (cf., Fox 1988, and references therein). In suprathermal electron-impact dissociation, most of the energy is carried away by the electron, and the energy that appears as translation has been found to be of the order of 1 eV (cf., Fox and Dalgarno 1979).

Exothermic ion-neutral and neutral-neutral reactions can be a significant source of heating for the ions and neutrals. The energies of the atomic products are determined by conservation of momentum and energy, but if there are molecular products, some of the available energy can appear as vibrational excitation. That fraction depends on the mechanism of the reaction, and is generally greater for reactions that proceed via a collision complex than those that proceed via a direct insertion/decomposition mechanism. Energy tends also to be deposited in vibration when a new bond is formed. In quenching of metastable species, such as $O(^1D)$, especially those that proceed via the formation of a collision complex, a significant (usually statistical) proportion of the energy can appear as vibrational excitation of the molecular products.

The most important reactions for heating on Venus and Mars are generally dissociative recombination reactions (see (8)). DR reactions tend to be very exothermic, and are the main loss process for ions whose parent neutrals have low ionization potentials. For DR of diatomic molecules, all the exothermicity that does not appear as electronic excitation appears as heat.

Fox (1988) computed the heating rates and efficiencies for a high solar activity model of Venus. The heating rates due to various processes are shown in Fig. 9. It can be seen that the most important source of heating is the DR reaction of the major molecular ion, O_2^+, above about 130 km. Below that altitude the most important sources of heat are almost equally photodissociation and quenching of metastable species. Electron impact dissociation and chemical reactions other than DR or quenching of metastable species are unimportant. Altitude profiles of resulting heating efficiencies are shown in Fig. 10a. The heating efficiency curve labeled "A" is for the standard model, and that labeled "B" is a lower limit. The lower limit model is based on extreme assumptions about the fraction of energy being deposited

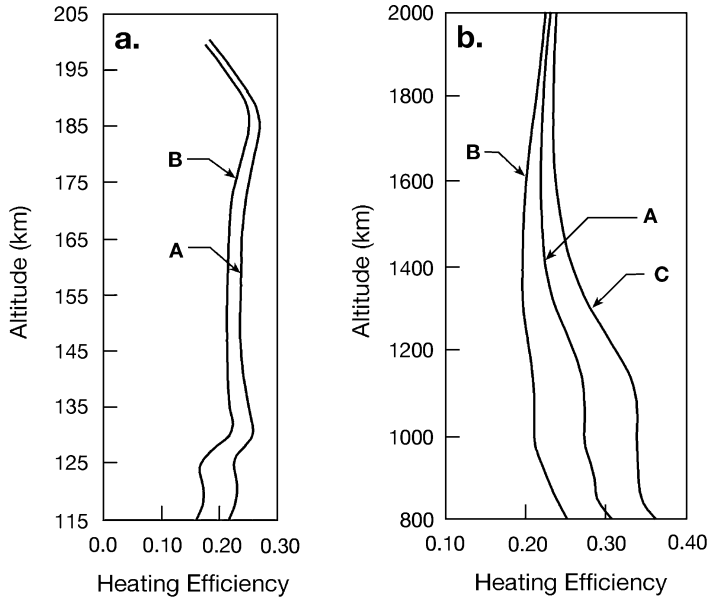

Fig. 10 Altitude profiles of heating efficiencies in the atmospheres of (**a**) Venus (adapted from Fox 1988) and (**b**) Titan (Fox and Yelle, unpublished calculations). The *curves labeled A* are from the standard models; those *labeled B* are lower limits. The *curve labeled C* in (**b**) is the upper limit for the Titan model (see text)

as vibrational excitation. The heating efficiencies range from 16 to 22% at altitudes near 100 km. A similar model for Mars exhibits heating rates and efficiencies that are comparable to those obtained for Venus (Fox et al. 1995).

By contrast, the heating rates on Titan are not dominated by DR reactions, partly because the dominant ions have been "processed more", that is, they have been transformed via many ion–molecule reactions before they can recombine. In addition, since most of the DR reactions are of polyatomics, some of the exothermicity may appear as vibration of the fragments produced. DR of N_2^+ is not an important heat source because N_2 has a high ionization potential, and therefore in the region near and for a significant distance above the main ion peak, N_2^+ tends to destroyed by ion–molecule reactions, rather than by DR. The main sources of heat are found to be photodissociation of N_2 and CH_4, and neutral-neutral chemical reactions. The standard "best guess" and upper and lower limits for the heating efficiencies on Titan are presented in Fig. 10b. These heating efficiency profiles correspond to different assumptions about the fraction of the exothermicities that appears as vibrational excitation in different processes. For example, in neutral-neutral and ion-neutral reactions, fractions of 60%, 40% and 80% are assumed for the standard, upper limit and lower limit models. The heating efficiencies are found to be in the range 25–35% at the lower boundary, and decrease with altitude to values near 22% at the top boundary of the model near 2000 km.

Roble et al. (1987) computed the heating efficiencies in the terrestrial thermosphere, and reported values that increased from 30% at about 100 km to $\sim$ 55% near the F_1 peak ($\sim$ 175 km) and then decreased to $\sim$ 30% near the exobase at 400–500 km. The main sources of heat for the earth are similar to those for Titan, and are photodissociation of O_2 in the Schumann-Runge continuum, and exothermic neutral–neutral reactions. The heating rates are significantly larger than those for Venus and Mars. The reasons for this are various,

but may be related to the fact that the major metastable species in the terrestrial ionosphere ($N(^2D)$ and $O(^1D)$) have long radiative lifetimes and are therefore quenched before they can radiate. The major metastable species produced on Venus and Mars, $CO(a^3\Pi)$, is characterized by a short radiative lifetime that exhibits a strong dependence on vibrational and rotational levels, and is in the range $\sim 3-150$ ms (e.g., Jongma et al. 1997). The $CO(a^3\Pi)$ state therefore mostly emits to the ground $X^1\Sigma$ state, producing the Cameron bands, before it can be quenched.

Also, the major species on Venus and Mars, CO_2, is a triatomic molecule. Its interaction with photons and electrons, and its chemical reactions, produce more molecular species for which the exothermicity can be taken up as vibrational excitation, than do reactions of O_2 and N_2 in the terrestrial atmosphere.

2.13 Auger Electrons and Characteristic X-rays

Measurements of doubly charge ions in the terrestrial thermosphere began with the Atmosphere Explorer in the mid 1970's, and in the Venus ionosphere by Pioneer Venus beginning in 1978. Since then, many models of altitude profiles of doubly charged ions densities have been constructed. The first studies were of O^{++} in the terrestrial and Venus atmospheres. More recently, studies of O^{++} and doubly charged molecular ions on other bodies have been carried out. The mechanisms for the production and loss of these ions are uncertain. The production processes include double valence shell ionization and Auger ionization, which may be produced by absorption of X-rays or by impact of very energetic particles. Signatures of Auger ionization have been identified in suprathermal electron flux measurements or predicted by models. Little is known about the loss processes for doubly charged ions, which complicates their modeling.

In addition, measurements of X-rays from various solar system bodies have been made, and their sources have been modeled. We describe the ways in which X-rays interact with atmospheric species, the cross sections for various competing processes, and the mechanisms for emission of X-rays that have been identified for various solar system bodies. We begin by describing the Auger effects and the production of characteristic X-rays.

Most atmospheric molecules are made up of atoms with atomic numbers $Z < 10$, and therefore only the K-and L-shells, defined as those characterized by principal quantum numbers $n = 1$, and $n = 2$, respectively, are populated in the ground states. The ground state of the noble gas He ($Z = 2$) has a filled K-shell with electron configuration $1s^2$; Ne ($Z = 10$) has filled K and L shells with electron configuration $1s^2 2s^2 2p^6$. Ar ($Z = 18$), a minor constituent in planetary atmospheres, has electrons in the ($n = 3$) M-shell; its ground state electron configuration is $1s^2 2s^2 2p^6 3s^2 3p^6$. Metals and other atoms that are formed from ablation of meteors in the mesospheres/thermospheres of planets also have electrons in levels with principal quantum numbers greater than 2. These atoms include, for example, Na (11), Mg (12), Si (14), Ca (20), and Fe (26), where the atomic numbers Z are shown in parentheses. Meteoric ion layers are present in all planetary atmospheres with substantial neutral densities.

The first ionization potentials of atoms and molecules, which are listed in Table 1, pertain to the ejection of outer shell electrons, which are fairly loosely bound. An inner K-shell or "core" ($1s$) electron can be ejected from an atom by absorption of an energetic photon or via a collision with an energetic electron. For atoms with atomic numbers greater than 4, the core-ionizing photons must be in the X-ray region of the spectrum, and the impinging electrons must be characterized by energies of the order of kilovolts.

After the ejection of the core electron, an electron in the L-shell may then make a transition to the $1s$ orbital. Selection rules for one-electron jumps (i.e., $\Delta\ell = \pm 1$) require that

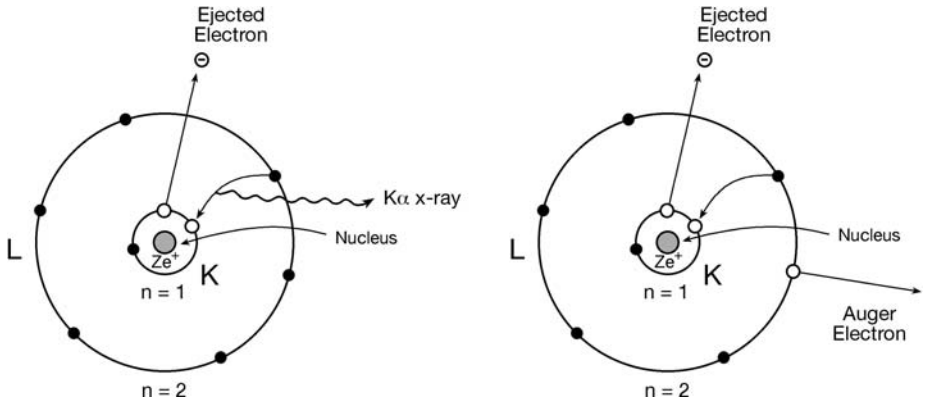

Fig. 11 Cartoon that represents the production of characteristic X-rays and Auger electrons. Only the K and L shells are shown. (*Left*) Characteristic X-rays are produced when absorption of an X-ray photon or energetic charged particle causes the ejection of a K-shell electron (*labeled "Ejected electron"*). An outer shell electron the makes transition to fill the hole in the inner shell. In this process, the excess energy is carried away by a $K\alpha$ X-ray. The ion is left in a singly ionized state. (*Right*) Auger electrons are produced by a similar sequence, except that the excess energy released in reorganization of the ion is carried away by an energetic "Auger" electron, which leaves the ion in the ground or an excited doubly ionized state

this electron be a $2p$ electron. The energy released in the decay of the core ionized state of the ion may be carried away by a characteristic X-ray of approximate energy,

$$E = 13.6(Z-1)^2\left(\frac{1}{{n_1}^2} - \frac{1}{{n_2}^2}\right)\text{eV}. \tag{25}$$

In this equation n_1 is the principal quantum number of the ejected electron and n_2 is the principal quantum number of the valence electron that replaces the inner electron. The characteristic X-ray is designated as "Kα" for $n_1 = 1$ and $n_2 = 2$. The English physicist H. G. C. Moseley studied this effect, which allowed him to determine the atomic numbers of many elements. This simple formula (25) yields energies of 255, 367, 499 and 2947 eV for the Kα X-rays for the atmospherically important atoms C, N, O, and Ar, respectively. If an atom has electrons in the shells with $n \geq 3$, it may, after ejection of an electron from the L-shell, produce a characteristic $L\alpha$ X-ray, which corresponds to $n_1 = 2$ and $n_2 = 3$ in (25). Kβ X-rays may also be emitted, if, after core ionization, an electron from the $n = 3$ (M-shell) drops down to fill the core hole; this corresponds to $n_1 = 1$ and $n_2 = 3$ in (25).

Alternatively, as the valence electron drops down to fill the vacancy in the K-shell, the excess energy may be carried away by the ejection of an outer shell electron, leaving the ion in a doubly ionized state. This ejected "Auger electron" is named after the physicist Pierre Auger, who discovered the phenomenon in the 1920's. These alternatives for relaxation of a core-hole ion are illustrated in Fig. 11. Alternatively, a related phenomenon, the radiative Auger process, may take place; here the excess energy is shared by the Auger electron and a simultaneously emitted photon (e.g., Mühleisen et al. 1996; Penent et al. 2005). For light elements, such as those that are found in the atmospheres of the planets, the Auger process is more important than the emission of characteristic X-rays, while the reverse is true for heavy elements. This is due to the increasing importance of photon emission as the atomic number increases, rather than to a decrease in the probability of ejection of an Auger electron (e.g., Condon and Shortley 1964). Krause (1979) has summarized the X-ray emission and Auger yields for K and L shells for atoms with $5 \leq Z \leq 110$, and showed that they are

equally probable for an atomic number of about 31. The Auger yields are 0.997, 0.995, and 0.992, and 0.882 for C, N, O and Ar, respectively. The thresholds for core ($1s^{-1}$) ionization of C, N, O and Ar are 291 eV (42.6 Å), 404.8 eV (30.6 Å), 538 eV (23.0 Å), and 3203 eV (3.87 Å), respectively, (e.g., Verner and Yakovlev 1995) and the Kα X-rays are characterized by wavelengths of 43.7, 30.9, 23.3, and 3.87 Å, respectively (Lide 2008).

We shall describe the details of these processes, specifically for atomic oxygen in the text that follows. The K-shell ionization of O by an X-ray or keV electron can be represented by

$$\mathrm{O}(1s^2s^22p^4) + (h\nu, e^*, [E > 538\ \mathrm{eV}]) \rightarrow \mathrm{O}^{+*}(1s2s^22p^4) + (e, 2e), \tag{26}$$

where O^{+*} represents a core-hole ion. In (26) the electron configurations of the ground state of the neutral and of the core-ionized ion are shown explicitly. After the ejection of the $1s$ electron, an outer L-shell electron may make a transition to the inner shell to fill the vacancy left by the ejected electron; this may be followed by the emission of a characteristic $K\alpha$ X-ray photon, e.g.,

$$\mathrm{O}^{+*}(1s2s^22p^4) \rightarrow \mathrm{O}^{+}(1s^22s^22p^3) + h\nu\ (\sim 23.6\,\text{Å}). \tag{27}$$

In the competing Auger process, after the ejection of the core electron, as the outer shell electron makes a transition to fill the core hole, the excess energy may be carried away by emission of an Auger electron from an outer shell, e.g.,

$$\mathrm{O}^{+*}(1s2s^22p^4) \rightarrow \mathrm{O}^{++}(1s^22s^22p^2) + e\,(\text{Auger}). \tag{28}$$

The energy of the Auger electron may be approximated as that of the $K\alpha$ X-ray minus the binding energy of the $n = 2$ electron. For O^+, the binding energy of the outer electron is approximately equal to the second ionization potential, ~ 35 eV, so that the Auger electrons are expected to have energies of about 500 eV.

This energy is, however, only an approximation. In fact, the core excited O^{+*} ion with electron configuration ($1s2s^22p^4$) ion actually corresponds to any of four electronic states with term symbols ${}^4P_{5/2,3/2,1/2}$, ${}^2P_{3/2,1/2}$, ${}^2D_{5/2,3/2}$ and ${}^2S_{1/2}$. Only the ${}^4P$ and ${}^2P$ states, however, have been observed experimentally from the $\mathrm{O}({}^3P)$ ground state (e.g., Petrini and de Araújo 1994). The energies of the ${}^2P_{3/2}$ and ${}^2P_{1/2}$ states have been computed by Lohmann and Fritzsche (1996) to lie 4.675 and 4.708 eV, respectively, above the lowest ${}^4P_{5/2}$ state. The ${}^4P_{3/2}$ and ${}^4P_{1/2}$ fine structure levels lie 0.04 eV and 0.053 eV, respectively, above the ${}^4P_{5/2}$ level.

The $K\alpha$ X-rays may arise from any of ten dipole allowed transitions from the two observed core-excited O^+ states to the three electronic states characterized by the ground state electron configuration $1s^22s^22p^3$, including the ground $\mathrm{O}^+({}^4S^{\mathrm{o}}_{3/2})$, and the excited $\mathrm{O}^+({}^2D^{\mathrm{o}}_{5/2,3/2})$, and $\mathrm{O}^+({}^2P^{\mathrm{o}}_{3/2,1/2})$ states; the energies of the latter two states are about 3.32 and 5.02 eV, respectively, above the ground state. The allowed radiative transitions between the core hole upper O^+ states and the lower states with the ground state electron configuration obey the dipole selection rules for radiative transitions: $\Delta S = 0$, $\Delta L = 0, \pm 1$; $\Delta J = 0, \pm 1$; $L = 0 \nleftrightarrow L = 0$; $J = 0 \nleftrightarrow J = 0$; e $\leftrightarrow$ o). Thus the X-rays produced in dipole-allowed transitions will be characterized by slightly different energies and intensities, and the $K\alpha$ "line" actually represents a series of closely spaced lines.

In the Auger process (see (28)) a radiationless transition takes place between the core hole ${}^4P$ and ${}^2P$ states of O^+ and the final O^{++} states. The end state with electron configuration $\mathrm{O}^{++}(1s^22s^22p^2)$ comprises three electronic states ${}^3P$, ${}^1D$, and ${}^1S$ with Auger electron energies in the range 492–498 eV; six states comprise the O^{++} final state with